Unconventional Photocurrents from Surface Fermi Arcs in Topological Chiral Semimetals

Guoqing Chang[1,*] Jia-Xin Yin,[1] Titus Neupert,[2] Daniel S. Sanchez,[1] Ilya Belopolski,[1] Songtian S. Zhang,[1] Tyler A. Cochran,[1] Zǐjiā Chéng,[1] Ming-Chien Hsu,[3] Shin-Ming Huang,[3] Biao Lian,[4] Su-Yang Xu,[1,5] Hsin Lin,[6] and M. Zahid Hasan[1,7,†]

[1]*Laboratory for Topological Quantum Matter and Advanced Spectroscopy (B7), Department of Physics, Princeton University, Princeton, New Jersey 08544, USA*
[2]*Department of Physics, University of Zurich, Winterthurerstrasse 190, 8057 Zurich, Switzerland*
[3]*Department of Physics, National Sun Yat-Sen University, Kaohsiung 804, Taiwan*
[4]*Department of Physics, Princeton University, Princeton, New Jersey 08544, USA*
[5]*Department of Chemistry and Chemical Biology, Harvard University, Cambridge, Massachusetts 02138, USA*
[6]*Institute of Physics, Academia Sinica, Taipei 11529, Taiwan*
[7]*Materials Sciences Division, Lawrence Berkeley National Laboratory, Berkeley, California 94720, USA*

The nonlinear optical responses from topological semimetals are crucial in both understanding the fundamental properties of quantum materials and designing next-generation light sensors or solar cells. However, previous work focused on the optical effects from bulk states only, disregarding the responses from topological surface states. In this Letter, we propose a new surface-only photocurrent response from chiral Fermi arcs. Using the ideal topological chiral semimetal RhSi as a representative, we quantitatively compute the photogalvanic currents from Fermi arcs on different surfaces. By rigorous crystal symmetry analysis, we demonstrate that Fermi arc photogalvanic currents can be perpendicular to the bulk injection currents regardless of the choice of materials surface. We then generalize this finding to other cubic chiral space groups and predict material candidates. Our theory reveals a powerful notion where common crystalline symmetry can be used to completely disentangle bulk and surface optical responses in many conducting material families.

Crystalline symmetries play a fundamental role in determining the electronic and optical properties of topological materials [1–6]. Materials in the same space groups may exhibit similar quantum properties due to the crystal symmetries they share [7–16]. By analyzing symmetry properties common to different space groups, one can generalize universal topological characteristics present across many material classes. For example, in nonmagnetic chiral crystals, real-space structural chirality robustly gives rise to largely separated Weyl-like chiral fermions with quantized Chern numbers in energy-momentum space which further induces many emergent quantum properties [16], including the exotic circular photogalvanic effect (CPGE) from Weyl fermions [17–28] and giant Fermi arc surface states [24,29–33]. The large photocurrents and broad light-sensitive energy windows of topological chiral crystals with Weyl-like fermions can be used to realize next-generation light sensors or solar cells beyond conventional semiconductors. Because of the potential applications, the photocurrents from Weyl-like semimetals have gained intense research interest in both theory and experiment. Both bulk Weyl fermions and surface Fermi arcs are important in Weyl-like semimetals. However, previous

works have considered only the nonlinear optical responses from bulk Weyl cones while overlooking the contributions from surface Fermi arcs [16–28].

In this Letter, we for the first time study a new photocurrent from surface Fermi arcs, which is induced by the chiral structures of Fermi arcs and surface crystalline-symmetry breaking on the boundary. We first quantitatively compute the CPGE photocurrents from the giant Fermi arcs in the ideal Weyl-like semimetal RhSi and then generalize our theory to topological cubic chiral crystals in space groups #195–#199 and #207–#214. Regardless of the choice of surface terminations, in cubic chiral crystals, the CPGE photocurrent from surface Fermi arcs can always be perpendicular to that from bulk Weyl cones. In general, it is challenging and nontrivial to disentangle the bulk and surface responses in topological metals [34–38]. For example, in transport, the quantum oscillations from the bulk Dirac or Weyl cones are often mixed with those from the surface [34]. Similarly, in spectroscopic experiments, one needs to conduct multiple measurements to distinguish the bulk signals and surface states [36]. Our theory shows that different symmetry constraints in bulk and on the surface allow circumstances

where the optical responses from surface and bulk states are completely disentangled.

The RhSi family has a nonsymmorphic cubic crystal structure in the space group $P2_13$ (#198) with the twofold screw rotations $S_{2x} = \{C_{2x}|0.5, 0.5, 0\}$, $S_{2y} = \{C_{2y}|0, 0.5, 0.5\}$, and $S_{2z} = \{C_{2z}|0.5, 0, 0.5\}$, which are related by the threefold diagonal rotation C_{3xyz}. This material class has been predicted as ideal Weyl semimetals with a fourfold degenerate chiral fermion at the Γ point and a sixfold degeneracy at the bulk Brillouin zone (BZ) corner R [24,29]. The electronic structure of RhSi in the presence of spin-orbit coupling (SOC) is plotted in Fig. 1(a). The angle-resolved photoemission spectroscopy (ARPES) measured constant energy contour on the (001) surface of RhSi is illustrated in Fig. 1(b), where the bulk Weyl or chiral fermions projected at $\bar{\Gamma}$ (Chern number $C = 4$ for the gap at the Fermi level) and $\bar{M}$ ($C = -4$) are connected by Fermi arcs spanning diagonally across the entire surface BZ [30–33]. Figure 1(c) shows the experimentally matched surface-state calculations of RhSi. In the absence of SOC, there are two sets of Fermi arc surface states. After turning on SOC, each set splits into two arcs of opposite spins. The energy dispersion along the red path in Fig. 1(c) cutting through the Fermi arcs is illustrated in

Fig. 1(d). At one k point, there are two sets of Fermi arcs, which suggests a potential light-absorption channel (indicated by the cyan arrow) within Fermi arcs. Because of the band bending near the crystal surface, Fermi arc surface states were predicted to exhibit the spiral structure [39,40]. Recent experiments have demonstrated the chiral structure of Fermi arcs in the RhSi family [30,31]. This potential light-absorption channel is possible because of the chiral (or helicoid) structure of Fermi arc surface states [30,40]. To better illustrate the chiral structure of Fermi arcs in RhSi, we plot the magnified view of the surface states around $\bar{M}$ in Fig. 1(e). The Fermi arc surface states spiral clockwise with increasing energy. As a result, the arc set 1 and arc set 2 can share the same momentum location at different energies.

This light-absorption channel of chiral Fermi arcs suggests that the optical responses of the RhSi surface can be dramatically different from that in bulk. Previous research has found that surface states can induce exotic surface photocurrents in insulators [41–43]. However, surface photocurrents have never been studied in topological Weyl semimetals, as previous work only considered the photocurrents induced by the bulk Weyl nodes [17–24,26–28]. Recent experiments have just shown evidence of the topological photocurrents in bulk of RhSi [28]. Therefore, it is crucial and timely to study the CPGE arising from giant Fermi arcs. We first study the CPGE where a circularly polarized laser induces an injection current in the ideal Weyl or chiral semimetal RhSi. In nonmagnetic materials, the circularly-polarized-light-induced CPGE currents can be written as [21,23,44,45]

$$\frac{dJ_i}{dt} = \beta_{i,j}(\omega)[\mathbf{E}(\omega) \times \mathbf{E}(\omega)^*]_j, \tag{1a}$$

$$\beta_{i,j}(\omega) = \frac{\pi e^3}{\hbar^2 V} \epsilon_{jkl} \sum_{\mathbf{k},n,m} f_{nm}^{\mathbf{k}} v_{\mathbf{k},nm}^i r_{\mathbf{k},nm}^k r_{\mathbf{k},nm}^l \delta(\hbar\omega - E_{\mathbf{k},mn}), \tag{1b}$$
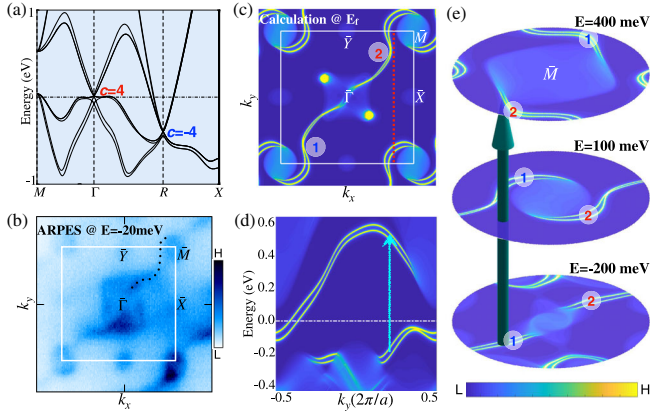

FIG. 1. Spiral Fermi arcs on the (001) surface of RhSi. (a) Electronic structure of RhSi in the presence of SOC. (b) ARPES-measured (001)-surface states of RhSi at 20 meV below the Fermi level. The Fermi arc surface states (indicated by the black dot line) stretch across the entire surface BZ along the xy direction. The white box indicates the first surface BZ. The color bar indicates the high (H) and low (L) spectral weight distributions on the surface. (c) First-principles calculations of (001)-surface states of RhSi at the Fermi level. Our calculations match the experimental measurements in panel (b). (d) The energy dispersion along the red dashed line indicated in panel (c). The white line indicates the Fermi level, and the cyan arrow shows a possible light-absorption channel between the Fermi arcs at different energies. (e) Helicoid Fermi arc structures around $\bar{M}$ at different energies. Fermi arcs spiral clockwise with increasing of energy, which induce the potential light-absorption channel indicated by the cyan arrow.

where $\mathbf{E}(\omega)$ is the electric field of the laser, the subscript j is the laser propagating direction, and i is the direction of injection current. $f_{nm}^{\mathbf{k}} = f_n^{\mathbf{k}} - f_m^{\mathbf{k}}$ is the difference of Fermi-Dirac distributions between bands n and m, $v_{\mathbf{k},nm}^i = \partial E_{\mathbf{k},nm}/\partial k_i$ is the difference of Fermi velocities, and $r_{\mathbf{k},nm}^l = i\langle n|\partial H_{\mathbf{k}}/\partial k_l|m\rangle$ is the matrix element of the Berry connection. β is the CPGE tensor and J is the injection current. To distinguish the bulk and surface photocurrents, we use different superscripts: β^b and J^b for the bulk, and β^s and J^s for the surface.

We first study the CPGE of RhSi with the laser along the principal axes: x, y, or z direction. For a generic point $\mathbf{k} = (k_x, k_y, k_z)$ in bulk, the screw rotation $S_{2z} = \{C_{2z}|0.5, 0, 0.5\}$ relates $\mathbf{k}$ to the partner $\mathbf{k}' = (-k_x, -k_y, k_z)$. The Fermi velocities and velocity matrix elements obey the

relations $v_{\mathbf{k}}^x = -v_{\mathbf{k}'}^x$, $v_{\mathbf{k}}^y = -v_{\mathbf{k}'}^y$, $v_{\mathbf{k}}^z = v_{\mathbf{k}'}^z$, $r_{\mathbf{k}}^x r_{\mathbf{k}}^y = r_{\mathbf{k}'}^x r_{\mathbf{k}'}^y$, $r_{\mathbf{k}}^y r_{\mathbf{k}}^z = -r_{\mathbf{k}'}^y r_{\mathbf{k}'}^z$, $r_{\mathbf{k}}^z r_{\mathbf{k}}^x = -r_{\mathbf{k}'}^z r_{\mathbf{k}'}^x$. From the integration of all the states in momentum space, we get $\beta_{x,z}^b = 0$ and $\beta_{y,z}^b = 0$. Owing to the cubic symmetry of the crystal, we further conclude that $\beta_{y,x}^b = 0$, $\beta_{z,x}^b = 0$, $\beta_{x,y}^b = 0$, and $\beta_{z,y}^b = 0$. The only nonzero bulk CPGE tensor elements are the diagonal terms $\beta_{x,x}^b$, $\beta_{y,y}^b$, and $\beta_{z,z}^b$ which are parallel to the laser direction. We now look at the photocurrents of the Fermi arcs on the surfaces perpendicular to the laser. On the (001) surface, the screw rotation S_{2z} is broken, since the spatial translation $\tau = (0.5, 0, 0.5)$ is no longer preserved on the boundary. Thus, $\beta_{x,z}^s$ and $\beta_{y,z}^s$ from Fermi arcs are generically nonvanishing. Similarly, $\beta_{y,x}^s$, $\beta_{z,x}^s$, $\beta_{x,y}^s$, and $\beta_{z,y}^s$ can also been nonzero. Therefore, on the (100), (010), and (001) surfaces of RhSi, the Fermi arc surface states induce photocurrents that are perpendicular to the laser direction.

The difference in the CPGE between the bulk and the (001) surface under a circularly polarized laser along the z direction can be visualized by the momentum-dependent circular optical absorption $|P_+|^2 - |P_-|^2$ [Fig. 2(a)]. Here, $P_\pm(\mathbf{k}) = 1/\sqrt{2}[P_x(\mathbf{k}) \pm iP_y(\mathbf{k})]$ is the transition matrix element of circularly polarized light, and $\mathbf{P}(\mathbf{k}) = \langle \phi_c(\mathbf{k}) | \hat{\mathbf{p}} | \phi_v(\mathbf{k}) \rangle$ is the interband transition [46]. Under the circularly polarized laser, bulk electrons at $\mathbf{k}$ and the rotation partner $\mathbf{k}'$ will be both excited [Fig. 2(a)] and generate opposite photocurrents $J_\perp^b$ (photocurrents perpendicular to the laser) which then cancel with each other [Fig. 2(b)]. In contrast, on the surface of the crystal, electron excitations only occur on one side of the BZ [Fig. 2(c)] and thus produce net nonzero injection currents [Fig. 2(d)]. We quantitatively compute the photocurrents from the Fermi arcs [Fig. 1(c)] on the (001) surface of RhSi. Our simulations are based on the Wannier functions derived from first-principles calculations. The photon-energy-dependent injection currents from the Fermi arc surface states of RhSi are plotted in Fig. 2(e). Unlike the bulk photocurrent in RhSi which has the quantized value, the surface photocurrents have no universal magnitude. The exact value of the surface photocurrent varies with the photon energy and the dispersions of Fermi arc surface states.

We now consider other second-order nonlinear optical responses in RhSi with the laser applied along the principal axes. One example is the shift current mechanism, which is a bulk photovoltaic effect induced by the coherent evolution of electron and hole wave functions [47]. The other case is the circular photon-drag effect where the photocurrent is generated by the transfer of momentum from light to charge carriers [48]. From a symmetry analysis, we find the bulk shift current is 0 under the circularly polarized laser along the principal axes (Supplemental Material B [49]). Similarly, the circular photon-drag current is also forbidden by symmetry in the bulk of cubic space group #198 (Supplemental Material C [48]) [53]. On the surface,
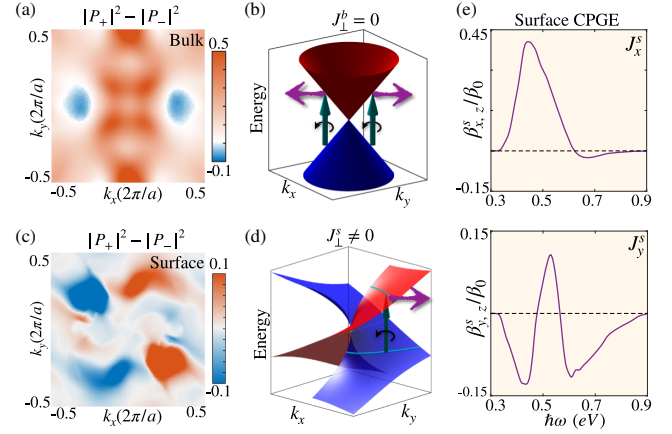

FIG. 2. CPGE in RhSi with laser normal to the (001) surface. (a) The momentum-resolved circular light absorption of RhSi at the $k_z = 0.1\pi/a$ plane. The $S_{2z} = \{C_{2z}|0.5, 0, 0.5\}$ rotation axis induces twofold light absorption from the bulk cone. (b) Schematics of photocurrent in the xy plane from the bulk Weyl cone. The cyan arrows indicate circularly polarized photons propagating along the z direction, and the purple arrows indicate light-induced photocurrents. Because of the existence of S_{2z} rotation symmetry in bulk, the photocurrent perpendicular to the laser $J_\perp^b$ vanishes. (c) The light absorption of the Fermi arc on the (001) surface in RhSi. Only time-reversal symmetry is still preserved. (d) Schematics of photocurrent from chiral Fermi arc surface states. The red and blue surfaces are two chiral Fermi arc surface states. A circularly polarized laser can only pump one side of the chiral arc, and thus generate a net nonvanishing photocurrent. (e) (001)-surface Fermi arcs induced CPGE photocurrents along the x and y directions in RhSi, respectively. $\beta_0 = \pi e^3/h^2$, where e and h are the electron charge and the Planck constant, respectively. The calculated CPGE photocurrents are obtained from the top four unit cells where Fermi arcs locate. When the light is not normal to the surface, the in-plane bulk photocurrent will be switched on. Because of the deep penetration of the laser [28], the in-plane bulk photocurrents can be much larger than the surface photocurrents.

due to the symmetry breaking, nonzero photon-drag and shift currents can be induced. All these surface effects, together with the CPGE (Fig. 2) will contribute to the surface photocurrents.

We now investigate the CPGE of RhSi when the laser is perpendicular to a generic (lmn) surface. The laser propagating along a generic direction can be decomposed under the three principal axes: $\mathbf{R} = [(l\hat{\mathbf{x}}, m\hat{\mathbf{y}}, n\hat{\mathbf{z}})/(\sqrt{l^2 + m^2 + n^2})]$. According to Eq. (1), the amplitude of photocurrents is proportional to the magnitude of the electric field. For cubic space group #198, the bulk injection currents induced by the circularly polarized laser along the $\mathbf{R}$ direction can be written as $\mathbf{J}^b = |J_\parallel^b|(l\hat{\mathbf{x}} + m\hat{\mathbf{y}} + n\hat{\mathbf{z}})$, which is parallel to the laser direction. On a generic (lmn) surface where the rotation symmetries are broken, surface photocurrents can be nonzero. The topological surface Fermi arcs can induce in-plane injection currents: $\mathbf{J}_\perp^s$. Here we use the (110) surface as the
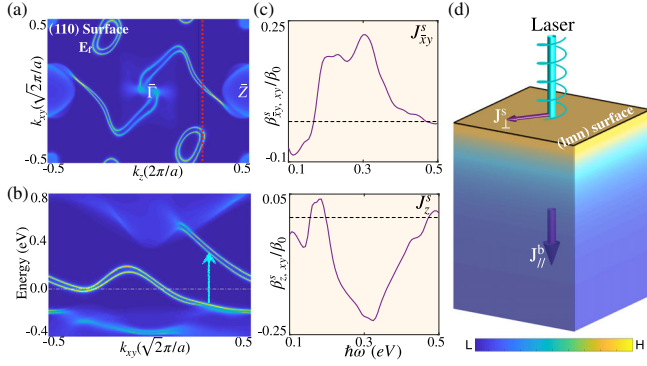
FIG. 3. CPGE from Fermi arcs on generic surfaces of RhSi. (a) (110)-surface states of RhSi at the Fermi level. Long Fermi arcs connecting projected chiral fermions at $\bar{\Gamma}$ and $\bar{Z}$ are observed. (b) Energy dispersions cutting through the Fermi arcs on panel (a). The cyan arrow indicates the possible light absorption between the (110)-surface Fermi arc surface states. (c) Numerical calculations reveal nonzero CPGE photocurrents from the (110)-surface Fermi arcs in RhSi under a laser perpendicular to the surface. The calculated CPGE photocurrents are obtained from the top four unit cells. (d) For any generic (lmn) surface of RhSi, under the circularly polarized laser perpendicular to the surface, the Fermi-arcs-induced CPGE photocurrents ($J_\perp^s$) are always perpendicular to the bulk CPGE photocurrents from chiral fermions ($J_\parallel^b$). The color bar indicates the high (H) and low (L) carrier density distributions from Fermi arc surface states. The photocurrents from the Fermi arcs should also be bounded on the surface, due to the surface localization of the Fermi arcs.

representative. Figure 3(a) shows the isoenergetic contours of the (110) surface, where long chiral Fermi arcs connect $\bar{\Gamma}$ and $\bar{Z}$. The energy dispersions of the chiral Fermi arc surface states are plotted in Fig. 3(b), with a

light-absorption channel indicated by the cyan arrow. Figure 3(c) shows the in-plane CPGE photocurrents of the (110) surface of RhSi. Figure 3(d) illustrates the CPGE of RhSi when the circularly polarized laser is perpendicular to a generic (lmn) surface. The photocurrents from chiral Fermi arc surface states, if any, are always perpendicular to the injection currents from the bulk cone. Therefore, by measuring CPGE photocurrents along different directions, one can detect contributions from bulk Weyl cones and surface Fermi arcs in RhSi separately. Our theory provides a rare example where optical responses from the topological bulk and surface states are fully disentangled in topological metals regardless of the surface terminations.

We then further generalize the theory of disentangled photocurrents from Fermi arc surface states and bulk chiral fermions into other materials. To realize the photocurrents from the surface Fermi arcs, the Weyl semimetals must satisfy the following criteria: (1) large nontrivial energy windows that allow an optical transition between two arcs at the same **k** points, and (2) low surface symmetries so that nonzero net surface photocurrents are allowed. In addition, in order to distinguish the photocurrents from Weyl cones and Fermi arcs, (3) additional crystal symmetries that eliminate bulk photocurrents perpendicular to the laser are required. Taking all three criteria into consideration, we find that topological cubic chiral crystals in space groups #195–#199 and #207–#214 are the best material candidates. The rotation symmetries of the cubic chiral crystals force the bulk CPGE photocurrents to be parallel to the laser. The unconventional multifold chiral fermions of cubic chiral crystals have a large separation in energy-momentum space, allowing long chiral Fermi arcs within a large energy window. We first check the nonsymmorphic

TABLE I. CPGE photocurrents of cubic chiral space groups and potential material candidates. Space groups #198, #199, #208, #210, and #212–#214 are nonsymmorphic chiral space groups, which include screw rotation axes indicated in the second column. Space groups #195–#197, #207, #209, and #211 are symmorphic chiral space groups. Columns 3 and 4 show the nonvanishing CPGE photocurrents when the laser is normal to the surface. The electronic structures of the potential material candidates are shown in the Supplemental Material D [49]. To sufficiently predict the Fermi arc photocurrents in these material candidates, detailed photocurrent calculations are needed in the future.

Space group	Related symmetries	(001)-surface	(110)-surface	Material candidates
198	$\{C_{2z}\|\frac{1}{2},0,\frac{1}{2}\}$	J_z^b, J_x^s, J_y^s	$J_{xy}^b; J_{\bar{x}y}^s, J_z^s$	AB (A = Co, Rh; B = Si, Ge); AuBe; AIX (X = Pd, Pt); BaPtY (Y = P, As)
199	$\{C_{2z}\|0,\frac{1}{2},0\}$	J_z^b	$J_{xy}^b; J_{\bar{x}y}^s, J_z^s$	
208	$C_{2z}; \{C_{4z}\|\frac{1}{2},\frac{1}{2},\frac{1}{2}\}$	J_z^b	$J_{xy}^b; J_{\bar{x}y}^s, J_z^s$	H_3X (X = P, As)
210	$C_{2z}; \{C_{4z}\|\frac{1}{4},\frac{1}{4},\frac{1}{4}\}$	J_z^b	$J_{xy}^b; J_{\bar{x}y}^s, J_z^s$	
212	$\{C_{2z}\|\frac{1}{2},0,\frac{1}{2}\}; \{C_{4z}\|\frac{3}{4},\frac{1}{4},\frac{3}{4}\}$	J_z^b, J_x^s, J_y^s	$J_{xy}^b; J_{\bar{x}y}^s, J_z^s$	Li_2BX_3 (X = Pd, Pt)
213	$\{C_{2z}\|\frac{1}{2},0,\frac{1}{2}\}; \{C_{4z}\|\frac{1}{4},\frac{3}{4},\frac{1}{4}\}$	J_z^b, J_x^s, J_y^s	$J_{xy}^b; J_{\bar{x}y}^s, J_z^s$	Mg_3Ru_2; $Na_4Sn_3O_8$; V_3Ga_2N; Nb_3Al_2N
214	$\{C_{2z}\|0,\frac{1}{2},0\}$	J_z^b	$J_{xy}^b; J_{\bar{x}y}^s, J_z^s$	La_3SiBr_3; La_3GaI_3
195–197	C_{2z}	J_z^b	$J_{xy}^b; J_{\bar{x}y}^s, J_z^s$	$La_4Re_6O_{19}$
207; 209; 211	$C_{2z}; C_{4z}$	J_z^b	$J_{xy}^b; J_{\bar{x}y}^s, J_z^s$	

chiral space groups. By analyzing the symmetry constraints, we find that space groups #198, #212, and #213 allow for the photocurrents from the (001) surface, since the nonsymmorphic symmetries are broken on the boundary. In contrast, in space groups #199 and #214, the CPGE from the Fermi arcs on the (001) surface is disallowed since the spiral translations are preserved on the boundary. Although the screw rotation S_{4z} is broken in space groups #208 and #210, the C_{2z} rotation is still preserved. Therefore, Fermi-arcs-induced photocurrents are also forbidden on the (001) surface of space groups #208 and #210. For the other surface terminations where there is no rotation symmetry, the (110) surface, for example, photocurrents from Fermi arcs are allowed in all nonsymmorphic cubic chiral space groups. Lastly, we study the Fermi arcs CPGE from symmorphic cubic chiral space groups: #195–#197, #207, #209, and #211. On the (001) surface, the rotation symmetry perpendicular to the plane is preserved. Thus, Fermi-arcs-induced photocurrents are forbidden. On other generic surfaces such as the (110) surface, Fermi arc photocurrents are allowed due to rotation symmetry breaking on the boundary. Following an extensive material search, we predict several new materials (Table I) which are ideal candidates to realize our theory.

Our theory works not only for topological materials listed in Table I, but it can also be applied to other trivial materials in the same space groups. Surface photocurrents can also be induced by trivial surface states. The difference between photocurrents from topological Fermi arcs and accidental trivial surface states is their robustness. The photocurrent from trivial surface states can be fully removed by changing surface terminations or chemical potential. In contrast, the photocurrents from Fermi arcs are robust against surface manipulations. The robustness of detectable photocurrents can be crucial for further potential applications. Our work can also help us understand other nonlinear optical experiments which could not be explained by bulk topology before [54], such as the robust edge photocurrent observed in WTe_2 [55] and giant surface second-harmonic generation in RhSi which may be induced from Fermi arcs [56].

To summarize, we have proposed new photocurrent responses from surface Fermi arc surface states induced by the lifting of symmetry constraints on the surface. We have first computed the bulk and surface CPGE photocurrents in RhSi from first-principles calculations, and then we have generalized our theory to other substantial material candidates in cubic chiral space groups. Our theory has provided an example where different symmetry constraints, symmetry protection in bulk and crystalline-symmetry breaking on the surface, can be used to disentangle bulk and surface photocurrents in many topological Weyl semimetals.

---

*Corresponding author.
guoqingc@princeton.edu
†mzhasan@princeton.edu

[1] M. Z. Hasan and C. L. Kane, Rev. Mod. Phys. **82**, 3045 (2010).

[2] X.-L. Qi and S.-C. Zhang, Rev. Mod. Phys. **83**, 1057 (2011).

[3] A. A. Burkov, Nat. Mater. **15**, 1145 (2016).

[4] M. Z. Hasan, S.-Y. Xu, and G. Bian, Phys. Scr. T **164**, 014001 (2015).

[5] A. Bansil, H. Lin, and T. Das, Rev. Mod. Phys. **88**, 021004 (2016).

[6] N. P. Armitage, E. J. Mele, and A. Vishwanath, Rev. Mod. Phys. **90**, 015001 (2018).

[7] L. Fu, Phys. Rev. Lett. **106**, 106802 (2011).

[8] S. M. Young, S. Zaheer, J. C. Y. Teo, C. L. Kane, E. J. Mele, and A. M. Rappe, Phys. Rev. Lett. **108**, 140405 (2012).

[9] H. Watanabe, H. C. Po, A. Vishwanath, and M. Zaletel, Proc. Natl. Acad. Sci. U.S.A. **112**, 14551 (2015).

[10] T. Bzdušek, Q. Wu, A. Rüegg, M. Sigrist, and A. A. Soluyanov, Nature (London) **538**, 75 (2016).

[11] Z. Wang, A. Alexandradinata, R. J. Cava, and B. A. Bernevig, Nature (London) **532**, 189 (2016).

[12] B. J. Wieder, Y. Kim, A. M. Rappe, and C. L. Kane, Phys. Rev. Lett. **116**, 186402 (2016).

[13] B. Bradlyn, J. Cano, Z. Wang, M. G. Vergniory, C. Felser, R. J. Cava, and B. A. Bernevig, Science **353**, aaf5037 (2016).

[14] G. Chang *et al.*, Phys. Rev. Lett. **119**, 156401 (2017).

[15] F. Schindler, A. M. Cook, M. G. Vergniory, Z. Wang, S. S. P. Parkin, B. A. Bernevig, and T. Neupert, Sci. Adv. **4**, eaat0346 (2018).

[16] G. Chang *et al.*, Nat. Mater. **17**, 978 (2018).

[17] P. Goswami, G. Sharma, and S. Tewari, Phys. Rev. B **92**, 161110(R) (2015).

[18] K. Taguchi, T. Imaeda, M. Sato, and Y. Tanaka, Phys. Rev. B **93**, 201202(R) (2016).

[19] H. Ishizuka, T. Hayata, M. Ueda, and N. Nagaosa, Phys. Rev. Lett. **117**, 216601 (2016).

[20] T. Morimoto, S. Zhong, J. Orenstein, and J. E. Moore, Phys. Rev. B **94**, 245121 (2016).

[21] C.-K. Chan, N. H. Lindner, G. Refael, and P. A. Lee, Phys. Rev. B **95**, 041104(R) (2017).

[22] M. Qiong et al., Nat. Phys. **13**, 842 (2017).

[23] F. de Juan, A. G. Grushin, T. Morimoto, and J. E. Moore, Nat. Commun. **8**, 15995 (2017).

[24] G. Chang et al., Phys. Rev. Lett. **119**, 206401 (2017).

[25] F. Flicker, F. de Juan, B. Bradlyn, T. Morimoto, M. G. Vergniory, and A. G. Grushin, Phys. Rev. B **98**, 155145 (2018).

[26] G. B. Osterhoudt et al., Nat. Mater. **18**, 471 (2019).

[27] J. Ma, Q. Gu, Y. Liu, J. Lai, P. Yu, X. Zhuo, Z. Liu, J.-H. Chen, J. Feng, and D. Sun, Nat. Mater. **18**, 476 (2019).

[28] D. Rees et al., arXiv:1902.03230.

[29] P. Tang, Q. Zhou, and S.-C. Zhang, Phys. Rev. Lett. **119**, 206402 (2017).

[30] D. S. Sanchez et al., Nature (London) **567**, 500 (2019).

[31] Z.-C. Rao et al., Nature (London) **567**, 496 (2019).

[32] D. Takane et al., Phys. Rev. Lett. **122**, 076402 (2019).

[33] N. B. M. Schröter et al., Nat. Phys. **15**, 759 (2019).

[34] A. C. Potter, I. Kimchi, and A. Vishwannath, Nat. Commun. **5**, 5161 (2014).

[35] P. Baireuther, J. A. Hutasoit, J. Tworzydło, and C. W. J. Beenakker, New J. Phys. **18**, 045009 (2016).

[36] S.-Y. Xu et al., Science **349**, 613 (2015).

[37] B. Q. Lv et al., Phys. Rev. X **5**, 031013 (2015).

[38] L. X. Yang et al., Nat. Phys. **11**, 728 (2015).

[39] S. Li and A. V. Andreev, Phys. Rev. B **92**, 201107(R) (2015).

[40] C. Fang, L. Lu, J. Liu, and L. Fu, Nat. Phys. **12**, 936 (2016).

[41] S. Thunich, L. Prechtel, D. Spirkoska, G. Abstreiter, A. Fontcuberta i Morral, and A. W. Holleitner, Appl. Phys. Lett. **95**, 083111 (2009).

[42] P. Hosur, Phys. Rev. B **83**, 035309 (2011).

[43] J. W. Mclver, D. Hsieh, H. Steinberg, P. Jarillo-Herrero, and N. Gedik, Nat. Nanotechnol. **7**, 96 (2012).

[44] J. E. Sipe and A. I. Shkrebtii, Phys. Rev. B **61**, 5337 (2000).

[45] T. Morimoto and N. Nagaosa, Sci. Adv. **2**, e1501524 (2016).

[46] T. Cao et al., Nat. Commun. **3**, 887 (2012).

[47] L. Z. Tan, F. Zheng, S. M. Young, F. Wang, S. Liu, and A. M. Rappe, npj Comput. Mater. **2**, 16026 (2016).

[48] E. L. Ivchenko, Optical Spectroscopy of Semiconductor Nanostructures (Alpha Science International, Harrow, UK, 2005).

[49] See Supplemental Material at http://link.aps.org/supplemental/10.1103/PhysRevLett.124.166404 for detailed first principles calculations, shift currents and circular photon-drag currents in RhSi, and additional materials candidates, which includes Refs. [50–52].

[50] G. Kresse and J. Furthmüller, Phys. Rev. B **54**, 11169 (1996).

[51] G. Kresse and D. Joubert, Phys. Rev. B **59**, 1758 (1999).

[52] J. P. Perdew, K. Burke, and M. Ernzerhof, Phys. Rev. Lett. **77**, 3865 (1996).

[53] V. A. Shalygin, M. D. Moldavskaya, S. N. Danilov, I. I. Farbshtein, and L. E. Golub, Phys. Rev. B **93**, 045207 (2016).

[54] G. Chang et al., arXiv:1906.03207; in Proceedings of the APS March Meeting, Denver, CO, 2020 (2020), http://meeting.aps.org/Meeting/MAR20/Session/B60.1.

[55] Q. Wang et al., arxiv:1910.04624

[56] J. Orenstein, in Proceedings of the APS March Meeting, Denver, CO, 2020 (2020), http://meeting.aps.org/Meeting/MAR20/Session/P55.1.